REPORT

The liquid state of FG-nucleoporins mimics permeability barrier properties of nuclear pore complexes

Giorgia Celetti[1,2,3]*, Giulia Paci[1,2,3]*, Joana Caria[1,2,3], Virginia VanDelinder[4], George Bachand[4], and Edward A. Lemke[1,2,3]

Nuclear pore complexes (NPCs) regulate all cargo traffic across the nuclear envelope. The transport conduit of NPCs is highly enriched in disordered phenylalanine/glycine-rich nucleoporins (FG-Nups), which form a permeability barrier of still elusive and highly debated molecular structure. Here we present a microfluidic device that triggered liquid-to-liquid phase separation of FG-Nups, which yielded droplets that showed typical properties of a liquid state. On the microfluidic chip, droplets were perfused with different transport-competent or -incompetent cargo complexes, and then the permeability barrier properties of the droplets were optically interrogated. We show that the liquid state mimics permeability barrier properties of the physiological nuclear transport pathway in intact NPCs in cells: that is, inert cargoes ranging from small proteins to large capsids were excluded from liquid FG-Nup droplets, but functional import complexes underwent facilitated import into droplets. Collectively, these data provide an experimental model of how NPCs can facilitate fast passage of cargoes across an order of magnitude in cargo size.

Introduction

The nuclear pore complex (NPC) is composed of multiple copies of roughly 30 different proteins (termed nucleoporins, or Nups) and regulates all nucleocytoplasmic transport. Small molecules can pass the NPC by passive diffusion. However, larger cargoes (smooth cutoff of ≈40 kD/4 nm in diameter; Timney et al., 2016) can pass through the NPC when bound to nuclear transport receptors (NTRs) that typically recognize nuclear localization signals (NLSs) or nuclear export signals (NESs) on the cargoes. Remarkably, even large preribosomal subunits, viral capsids, and mRNAs, with diameters almost equal to the central transport channel themselves, can pass the NPC barrier intact (Au and Panté, 2012; Babcock et al., 2004; Grünwald and Singer, 2010; Mor et al., 2010; Panté and Kann, 2002; Seisenberger et al., 2001; Tu et al., 2013).

Recent advances in structural biology combining X-ray crystallography, electron tomography, and mass spectrometry with integral modeling have yielded an impressive structural model of the NPC scaffold (Eibauer et al., 2015; Kim et al., 2018; Kosinski et al., 2016; Lin et al., 2016; Ori et al., 2013). Comparatively, very little structural insight is available for the actual transport channel, which even in highly resolved electron tomography showed up only as a large hole of >20 nm, because the tomogram generation process typically averages out unstructured regions. The central channel of the NPC is densely filled with multiple copies of about 10 different intrinsically disordered Nups that are rich in phenylalanine and glycine residues (FG-Nups). These FG-Nups form the NPC permeability barrier (Nehrbass et al., 1990; Ori et al., 2013; Ribbeck and Görlich, 2002). As the plasticity of FG-Nups inherent to their disordered nature prevents the application of most conventional structural biology approaches, their geometric arrangement and how the transport machinery works molecularly are still widely debated. With the physiological permeability barrier of the NPC being of submicroscopic resolution, much of our current knowledge and hypotheses are derived from in vitro studies using purified/reconstituted FG-Nup domain model systems (where the NPC anchoring site was removed). In solution, FG-Nups can adopt different conformations and supramolecular states and have also been shown to undergo liquid-to-gel and liquid-to-solid phase transitions to tough macroscopic hydrogels

[1]Biocentre, Johannes Gutenberg-University Mainz, Mainz, Germany;   [2]Institute of Molecular Biology, Mainz, Germany;   [3]Structural and Computational Biology Unit and Cell Biology and Biophysics Unit, European Molecular Biology Laboratory, Heidelberg, Germany;   [4]Center for Integrated Nanotechnologies, Sandia National Laboratories, Albuquerque, NM.

*G. Celetti and G. Paci contributed equally to this paper;   Correspondence to Edward A. Lemke: edlemke@uni-mainz.de;   George Bachand: gdbacha@sandia.gov;   Virginia VanDelinder: vvandelinder@gmail.com.

and amyloid-like fibers (Frey and Görlich, 2007; Ader et al., 2010; Yamada et al., 2010; Hough et al., 2015; Milles et al., 2013, 2015). Surface and channel grafted FG-Nups have been shown to display phenotypes ranging from polymer brushes to films (Eisele et al., 2013; Fisher et al., 2018; Fu et al., 2017; Jovanovic-Talisman et al., 2009; Ketterer et al., 2018; Lim et al., 2007; Moussavi-Baygi et al., 2011; Wagner et al., 2015; Zahn et al., 2016). The theorized permeability barrier models are similarly diverse. Convergence of the models has clearly been slowed down by the multifaceted nature of FG-Nups, as well as their high aggregation tendency, leading to different experimental outcomes.

In vitro phase separation assays have become widely used in the study of intrinsically disordered proteins. As phase separation occurs above a critical concentration, often a concentrated solution of FG-Nup in a denaturing buffer is rapidly diluted into a physiological condition. Additives such as trimethylamine N-oxide (TMAO, a small molecule osmolyte; Ferreon et al., 2012; Levine et al., 2015) or polyethylene glycol (PEG, a large molecule crowder; Annunziata et al., 2002) are frequently added to the solution to assist in in vitro phase separation assays. Often, adding those compounds is considered to better mimic the crowded in cellulo conditions, but the exact mechanism of those additives is not established in all cases. However, in general, they offer a convenient way to tune protein–protein versus protein–solvent interactions (Alberti et al., 2019), so that the proteins do not simply precipitate to an amorphous aggregate (a form of liquid-to-solid phase separation), which is commonly observed for highly aggregation-prone proteins. Analogously, FG-Nup hydrogels have been formed from either lyophilized powder or rapid dilution of concentrated denatured solution (Frey and Görlich, 2007; Konishi and Yoshimura, 2018; Milles et al., 2013; Milles and Lemke, 2011; Schmidt and Görlich, 2015). In FRAP experiments, hydrogel particles doped with fluorescent FG-Nups did not recover when bleached, revealing limited mobility in line with formation of a tough hydrogel state (Frey and Görlich, 2007; Konishi and Yoshimura, 2018; Schmidt and Görlich, 2015).

Particular attention has been given to the interaction properties between these hydrogel particles and various cargo proteins. Several studies on FG-Nup hydrogel particles have shown that they rapidly enrich with cargoes bearing a signal that is recognized by nuclear transport receptors such as Importin β (in facilitated import, the NLS binds to Importin α, which in turn binds to Importin β via its Importin β–binding [IBB] domain). In contrast, inert cargoes such as dextran (70 kD) or mCherry (without an NLS or IBB domain) are excluded from these particles (passive exclusion). The partition coefficient volume of inert cargoes exceeded the pure excluded volume effect of FG-Nups in the FG-Nup gel particle, and this permeability barrier effect was accounted for by hypothesizing the formation of a mesh structure that ultimately translates into mechanical stability, yielding a tough hydrogel (Ader et al., 2010; Frey and Görlich, 2007; Schmidt and Görlich, 2015).

Here we present a microfluidic device that controls the phase transition of FG-Nups on a millisecond time scale and their subsequent interaction with cargoes of interest under optical interrogation. The microfluidic device enabled us to perform rapid phase separation and direct interrogation of the properties of FG-Nup droplets on a previously unexplored time scale range. We determined that FG-Nups can undergo liquid-to-liquid phase separation, leading to a highly dynamic droplet state that obeys all characteristics of a liquid. Remarkably, the liquid state displayed NPC-like properties, as tested with cargoes of sizes spanning an order of magnitude.

Results and discussion

We selected the disordered domain of yeast FG-Nup49 (aa 1–249), as it contains multiple GLFG repeats. In metazoans, GLFG containing FG-Nup98 was found to be essential for creating reconstituted NPCs with functional permeability properties (Hülsmann et al., 2012; Schmidt and Görlich, 2015). Furthermore, FG-Nup49 has been previously characterized to be a hydrogel-forming Nup that exhibits permeability barrier–like properties (Milles et al., 2013). EM analysis of such FG-Nup49 macroscopic hydrogels showed a fiber network that, due to its dimensions (fibers partially thicker than 100 nm), was unlikely to be of physiological relevance and thus more likely to be a consequence of phase transition into a solid state (Milles et al., 2013). Such molecular aging of protein assembly states are also known from other phase-separating proteins (Lin et al., 2015; Patel et al., 2015).

Fig. 1 shows the design of the microfluidic device developed in this study. It is composed of two mixing regions (MI and MII; Fig. 1 A) and an optical interrogation region in which molecules flow along a snake-like channel for long observation (minutes; Fig. 1 D). In the mixing region MI, a highly concentrated solution of the FG-Nup49 in 4 M guanidinium hydrochloride (GdmHCl; arrow on the left in Fig. 1 B) flows from the sample inlet to the MI region (Fig. 1 A, pink square), where the protein solution is squeezed into a thin layer by the buffer stream containing PBS and 30% TMAO. We show in Fig. S1 that both PEG and TMAO help to tune phase separation of FG-Nups. The laminar flow mixing leads to rapid dilution of the GdmHCl and buffer exchange to physiological PBS buffer within milliseconds (Gambin et al., 2011; Lemke et al., 2009; Tyagi et al., 2014).

FG-Nup49 was doped with 500 nM of fluorescently labeled FG-Nup49 for whole-chip visualization using a 10× objective on an inverted epifluorescence microscope. As shown in Fig. 1, the microfluidic device enabled us to visualize the formation of FG-Nup droplets (elusive in coverslip assay procedures) and observe them for 20 min while they traveled along the 3-mm-long observation channel. The droplets displayed properties of a liquid state, including droplet coalescence, deformability, and fast recovery in FRAP experiments (Fig. 1, C–F). After the outlet, we typically detected (over extended periods of device operation) visible gel formation that ultimately led to clogging of the device; however, in the snake-like channels, we could observe droplets right after generation due to phase separation and follow the liquid droplets while traveling along the channel, which distinguishes this technology from simple coverslip assays.

To study whether the liquid state of the FG-Nups displays NPC-like properties, we designed a second mixing region (MII)
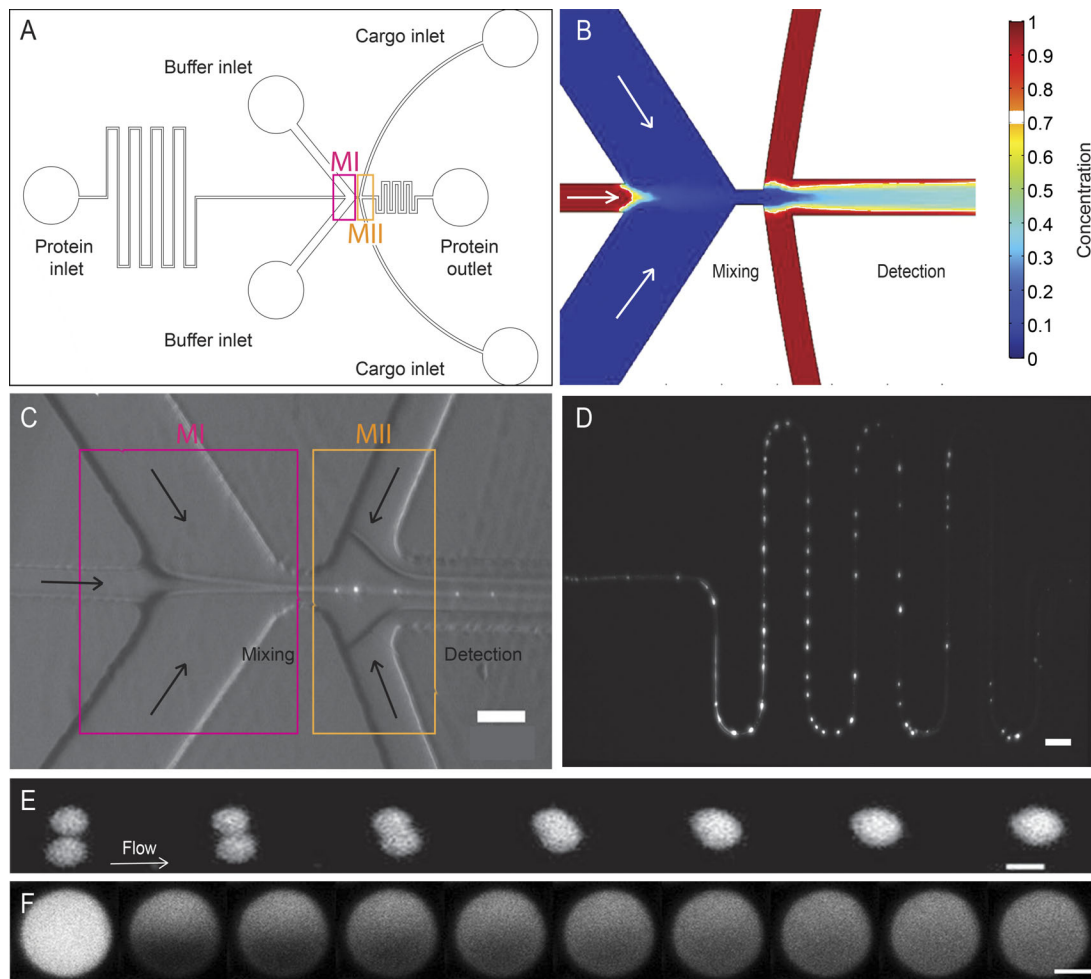
Figure 1. **Liquid–liquid phase separated FG-Nup49 droplets in the microfluidic device. (A)** Scheme of the microfluidic device/chip. **(B)** COMSOL color image (flow simulations, see Fig. S1 for details) of the working principle of the device. **(C)** First mixer of the device (MI) where the denatured FG-Nup protein solution is buffer exchanged into a physiological buffer, and the formation of droplets is triggered that then flow toward MII. The image shows a bright field view of the device overlaid with a fluorescent snapshot of FG-Nup49 droplet formation. **(D)** Fluorescence image of FG-Nup49 droplets flowing along the snake-like observation channel after their formation (10×, air objective, epifluorescence microscopy). Scale bar is 50 μm. **(E)** Snapshots of a coalescence event between two liquid FG-Nup49 droplets (20×, air objective, epifluorescence microscopy). Scale bar is 10 μm. **(F)** FRAP experiment of one droplet in the device (63×, oil objective, confocal microscopy). Each frame corresponds to a 2-s interval acquisition. Scale bar is 3 μm.

in the device (Fig. 1 A), where cargoes such as IBB-MBP-GFP (≈80 kD), preincubated with Importin β, could interact with the droplets. As detailed in Fig. S1, the flow rates in MII had to be below a limit to avoid shearing and/or squeezing of liquid droplets. Consequently, the biomolecules from the cargo inlet flowed at the sides of the channel parallel to the large droplets in the center, and cargo molecules reached the droplets over time by diffusion (Figs. 2 and S1). In Fig. 2, the first row shows the behavior of the respective cargo constructs in permeabilized cells assays with a reconstituted functional nuclear transport machinery. Permeabilized cell assays are commonly used to study cellular nuclear import machinery (Adam et al., 1990).

As shown in Fig. 2, A and B (whole microfluidic chip imaging using epifluorescence), IBB-MBP-GFP rapidly penetrated and enriched in the droplets only in the presence of Importin β (Fig. 2, A vs. B, and corresponding Videos 1 vs. 2). As an additional negative control, we used a variant of the GFP cargo bearing an M9 signal (M9-MBP-GFP ≈80 kD) and observed that

this protein did not enrich in droplets (Fig. 2 C and corresponding Video 3). M9 is another type of NLS that is not recognized by Importin β. The last row shows dot plots where the cargo enrichment of individual droplets was analyzed and plotted over distance traveled (refer to Materials and methods for droplet-by-droplet analysis). Consistent with the images, cargo enriched inside droplets only in Fig. 2 A, where a functional import complex could assemble. Additional experiments using another model cargo that agree well with these results are shown in Fig. S3.

We determined the average intradroplet FG-Nup49 concentration to be ≈4–5 mM (corresponding to ≈140 mg/ml; Fig. S1). This concentration was in good agreement with the estimated FG-Nup concentration of previously characterized FG-Nup hydrogels (Frey and Görlich, 2007). Assuming the partial specific volume for the polypeptide chain of 0.73 ml/g (Hinz 2012), we estimate that the FG-Nup itself amounted on average to 10% of droplet volume and the aqueous buffer to the remaining 90% of
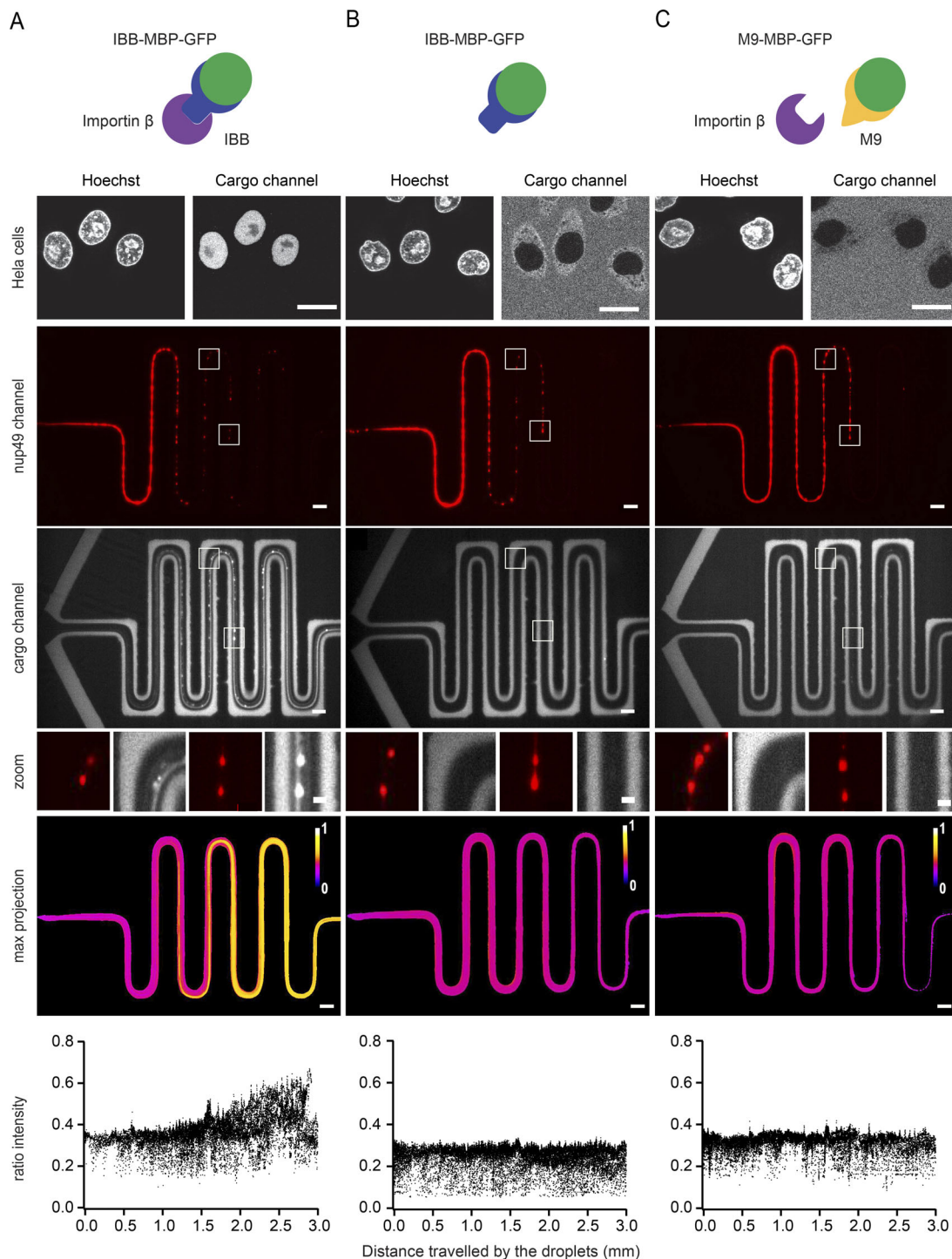
Figure 2. **Facilitated transport of MBP-GFP cargoes into FG-Nup49 droplets.** Epifluorescence microscopy of whole microfluidic device/chip. **(A)** Interaction between the IBB-MBP-GFP cargo and FG-Nup49 droplets in the presence of Importin β. **(B and C)** Two control experiments: the IBB-MBP-GFP cargo without Importin β and the M9-MBP-GFP cargo in the presence of Importin β. The rows of the figures are organized as follows. Top row: Confocal images of the respective cargo construct in permeabilized cells assays with a functional nuclear transport machinery. Second and third rows: Snapshot of the droplet channel (FG-Nup49), followed by a corresponding snapshot of the cargo channel. Fourth row: Two zooms corresponding to the white boxes in images above. Fifth row: Ratiometric maximum projection of an entire image series (see Fig. S2 for details on ratiometric analysis). Bottom row: Single-droplet analysis of the fluorescent cargo signals within the FG-Nup49 droplets while they travel along the device during each experiment. Briefly, droplets were segmented from the ratiometric video, and the intensity was estimated and plotted in relation to the droplet centroid position along the device. Each dot on the plots represents a single droplet. All rows: The FG-Nup49 droplets channel is displayed in red, the GFP cargo channel is in grayscale, and the ratiometric projections of the experiment (last row) show a colorimetric interaction of the cargo with the droplets. The more yellow/white the color, the more the cargo enriched inside the FG-Nup droplet. Scale bar is 50 µm. See corresponding Videos 1, 2, and 3 and details in Materials and methods for the ratiometric analysis. Scale bar in the zoom is 20 µm. Shown are exemplarily datasets from three technical replicates. In each dataset, >10,000 droplets are analyzed.

droplet volume (Fig. S1). Exclusion of inert cargoes from a droplet beyond the excluded volume of FG-Nup itself can be seen as a mimic of passive exclusion NPC-like permeability barrier properties (Schmidt and Görlich, 2015). In a coverslip experiment of hydrogel droplets, this can be easily quantified, as the fluorescence outside and inside the droplet can be directly compared under steady-state conditions.

Under the laminar flow conditions in our device, cargo molecules reached the droplets via slow diffusion, so that full immersion of the droplets in the cargo bath would be reached only in a channel ≈1 cm long (see Fig. S1 and Materials and methods). Therefore, it is not possible to transfer the experimental conditions from steady-state coverslip assays to our flow device. We thus performed three experiments to assay whether the liquid state displayed qualitatively permeability barrier–like properties with respect to passive exclusion. For these experiments, a confocal laser scanning microscope was used to image thin optical sections through the droplet, at the cost of smaller fields of view and slower image acquisition. We studied three effects. (1) The interaction of an M9-MBP-GFP fusion protein cargo with FG-Nup droplets: as shown in Fig. 3 A (and corresponding Video 4), the GFP cargo accumulated on the surface of the droplets more than inside, leading to a rim staining. (2) The small mCherry-12His (≈30 kD) showed a similar rim type of staining effect (Fig. 3 B and corresponding Video 5). The rim stainings were indicative of formation of a barrier, reminiscent to previously observed rim staining under steady-state conditions of other fluorescent protein cargoes that had limited ability to penetrate into hydrogel particles (Frey et al., 2018). (3) An mCherry (≈30 kD) without the His tag did not show the rim effect (Fig. 3 C and corresponding Video 6) and was excluded homogeneously from the liquid droplet. Together, these findings indicated that a hydrophobic part of the M9-MBP-GFP and mCherry-12His constructs interacted with the liquid droplet, but the hydrophilic properties of the rest of the cargoes prevented further penetration. For mCherry, a line profile analysis (Fig. 3, last row) indicated that more than ≈70% of inert cargo remained excluded in all tested cases. While an exact partition coefficient should not be extracted from those flow conditions (Fig. S1 and methods), all three experiments together strongly suggest that in the liquid state, an efficient permeability barrier was formed that displayed passive exclusion properties.

In a liquid state, FG-Nups remain flexible, and intermolecular bonds can be broken and formed on a very fast time scale, and should be able to accommodate large dynamics. As transport of large cargoes in principle requires megadaltons of protein mass to be moved (Paci and Lemke, 2019), we tested if the liquid state FG-Nup droplets could also enable facilitated import of a very large model cargo. We tested a previously used recombinant capsid from the MS2 bacteriophage (27 nm in diameter), which was covered with fluorescent dyes and NLSs and known to be an import cargo, as well as a capsid without NLSs as a negative control. We repeated the experiment for the MS2 capsid analogue to the IBB-MBP-GFP described above (Fig. 4). We observed precipitation during flow experiments. This complication limited our ability to compare the accumulation speed of such large cargo with respect to the much smaller model cargoes tested

above. We speculate that the fact that the capsid, which has ≈100 NLSs, could bind multiple Importin βs (which is itself a multivalent molecule) could lead to formation of larger aggregates. Regardless, it could be observed that fast import occurred only in the presence of MS2-NLS and Importin β/Importin α.

Our experiments present a laminar flow device able to generally study phase separation, applied here to specifically study FG-Nups. The addition of a second mixer (MII) right after the first mixer MI, which triggers phase separation and droplet formation, allowed us to follow how cargoes known from cell-based studies can enter the droplets while flowing along the snake-like optical interrogation channel. The device provided an exclusive look at the liquid state of FG-Nups before they mature into more solid states (tough hydrogel, amyloids, etc.), as could be seen from the occurrence of rapid coalescence (a signature of a liquid state) along the observation channel. In a liquid state, inter- and intramolecular contacts between proteins remain highly dynamic compared with more gel- or solid-like assemblies. The formation of a rather stable FG–FG meshwork, which translates to mechanical stability of a hydrogel, does not appear to be an essential requirement to yield basic NPC-like permeability barrier properties (Ader et al., 2010; Frey and Görlich, 2007). However, this does not exclude the possibility that a highly dynamic meshwork could be responsible for the observed behaviors. In fact, we know from other biological condensates that liquid states can also obey effective mesh sizes (Wei et al., 2017). The highly dynamic nature intrinsic to a liquid phase also provides a good explanation for how cargoes across different sizes and even large viruses can enter the NPC. In our solution experiments yielding liquid droplets, the FG domain was not tethered to a surface or scaffold. In contrast, previous studies on grafted FG-Nups maintain many of the geometrical aspects of the NPC, and thus a direct comparison is not possible. However, those studies also have not yet converged to a single interpretation or transport model (Eisele et al., 2013; Fisher et al., 2018; Fu et al., 2017; Jovanovic-Talisman et al., 2009; Ketterer et al., 2018; Lim et al., 2007; Moussavi-Baygi et al., 2011; Wagner et al., 2015; Zahn et al., 2016).

While the dimension of a polymer is typically different in a liquid state compared with a brush state (Schäfer, 1999), both systems are (in the case of FG-Nups) compatible with the existence of highly dynamic states. Since the disordered region of FG-Nups can easily be >500 aa, formation of a highly dynamic matrix inside the NPC can be envisioned, even if the FG-Nups are tethered at one end. We note that liquid, gel, solid, and even expanded conformations as in a brush state are part of a continuum and can be very close neighbors in a phase diagram of heteropolymers, such as intrinsically disordered FG-Nups. On the phase boundaries, more than one phase can even coexist, and thus identifying the exact states in cellulo will remain challenging. While the liquid state can recapitulate key properties of physiological NPC function in vitro, we currently lack the technology to directly probe if the FG-Nups in the nanosized NPC barrier are liquid. One important question that now arises is how a physiological permeability barrier could be kept in the liquid state in vivo, since in vitro the liquid state is transient and ages to more solid states. One possibility is that different
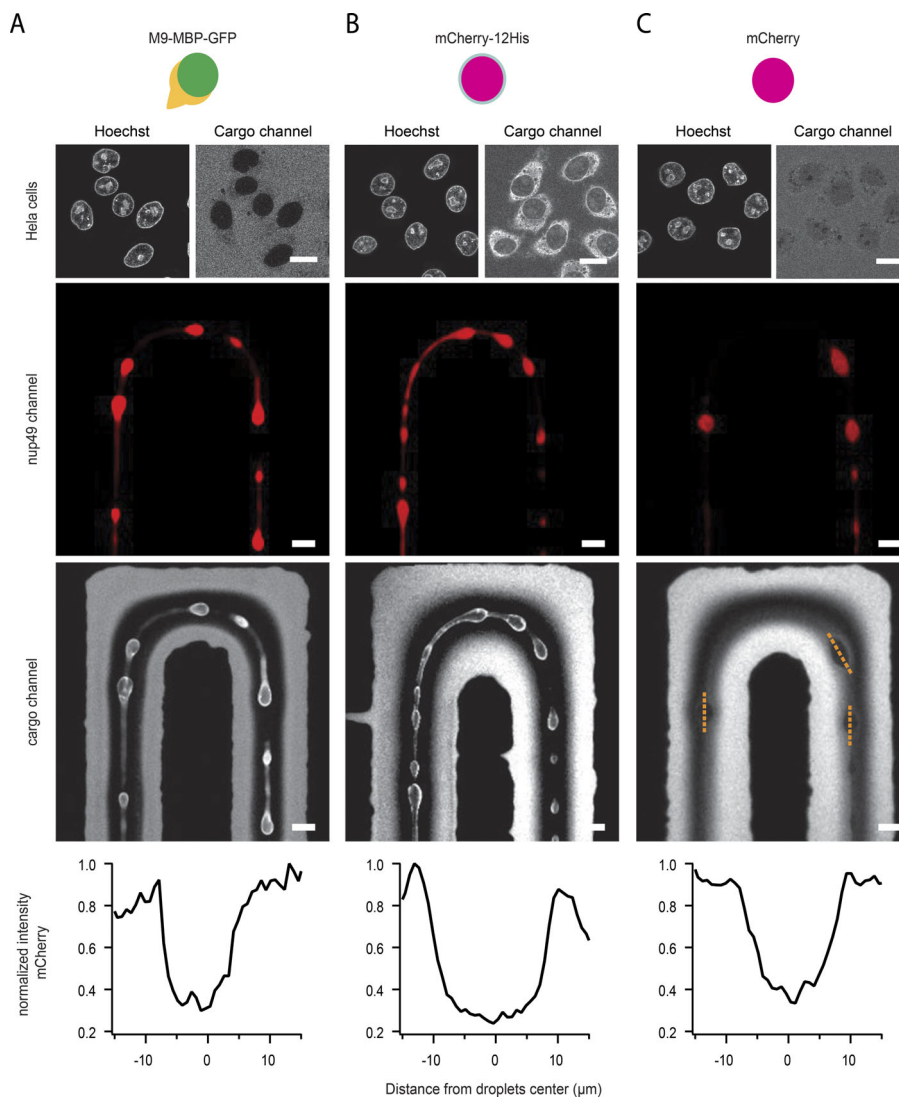
Figure 3. **Passive exclusion properties of the liquid state of FG-Nup49.** Confocal microscopy of flowing droplets. **(A–C)** The passive exclusion of the three cargoes from the FG-Nup49 droplets. The first row (A) shows confocal images in permeabilized cell experiments analogous to Fig. 2. The confocal images below (B) show the FG-Nup49 droplets represented in red and the cargo in grayscale. The last row shows the line profiles of the three droplets in the mCherry experiment (C) along the orange lines. All experiments were performed in the absence of NTRs. Fig. S3 shows a validation that an IBB-mCherry cargo in the presence of Importin β is imported. Scale bar is 20 µm. See corresponding Videos 4, 5, and 6.

FG-Nups might stabilize the liquid state when combined together. Analogues for this hypothesis are ubiquitous in the literature, e.g., the inhibition of amyloid-β plaques or aggregates by α-synuclein (Bachhuber et al., 2015) or mixing of the intrinsically disordered protein FUS with EWS or TAF15 (Marrone et al., 2019). In the future, more complex device designs that have additional mixers for on-chip preparation of different FG-Nups may address this question. This could explain why NPCs are so complex in vivo (10 different FG-Nups and an additional 20 scaffold Nups, which in part also contain intrinsically disordered regions; Teimer et al., 2017), with little sequence conservation of the disordered part across species, even though the fundamental properties of the NPC permeability barrier can be recapitulated from only one to a few components (Hülsmann et al., 2012; Strawn et al., 2004).

Future reimplementations of the device could also simultaneously study droplet microrheology (Elbaum-Garfinkle et al., 2015), which could provide a more refined look at the material properties of the droplets over long time periods. Those might also enable a quantitative comparison between the permeability barrier properties of hydrogels versus liquid droplets under same conditions. Recent studies have suggested an integral role of NTRs as part of the permeability barrier (Kapinos et al., 2017; Lowe et al., 2015). Microrheology measurements could also investigate the permeability barrier properties over material states to assay if the presence of NTRs affect the molecular architecture of the droplet. Finally, implementation of a third mixer could also be used to study cargo release from droplets, for example, when perfusing droplets with RanGTP, so that all steps of nucleocytoplasmic transport (docking, barrier passage, and undocking) can be studied on the microfluidic device.

Materials and methods

Sample preparation

FG-Nup49 aa 1-249 was purified as previously reported (Milles et al., 2013). Briefly, it was cloned as N-terminal fusion proteins with an Intein-CBD-12His tag. Cells were grown in terrific broth medium containing 50 µg/ml of ampicillin at 37°C, and protein expression was induced with 0.02% arabinose at OD_{600} = 0.4–0.8. After 4 h at 37°C, cells were harvested by centrifugation. Cell pellets stored at –80°C were resuspended in 4× PBS, pH 8,
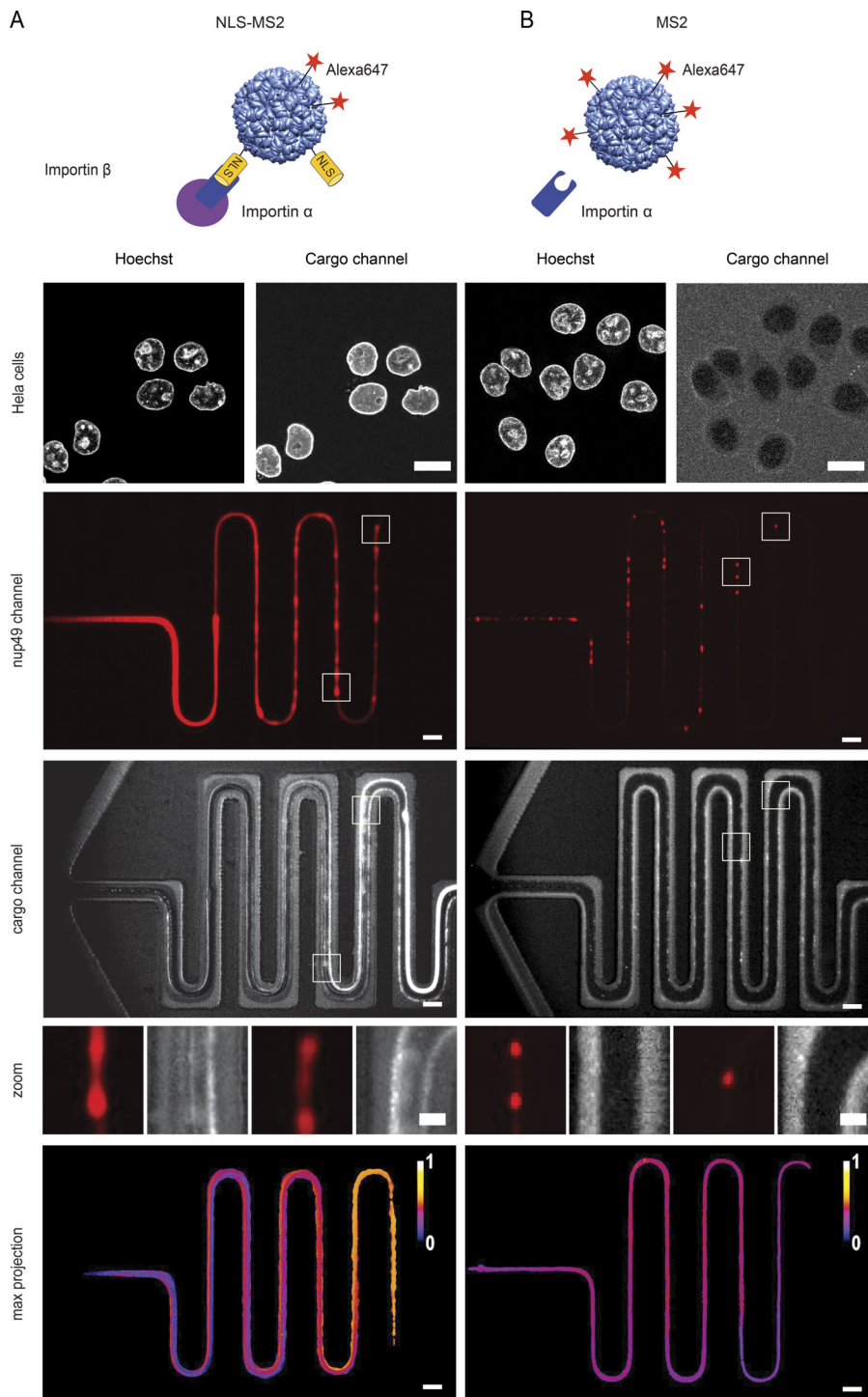
Figure 4. **Facilitated transport of MS2 capsids into FG-Nup49 droplets.** Epifluorescence microscopy of whole device. Panels are organized analogously to Fig. 2. **(A)** Interaction between the MS2-NLS capsid and the FG-Nup49 droplets in the presence of Importin α/Importin β, showing the cargo entering into the droplets (see also zoom). **(B)** The negative experiment: MS2 capsid without NLSs. For all rows: FG-Nups49 droplet channel is displayed in red, MS2 cargo channel is in grayscale, and the ratiometric projection of the full experiment shows colorimetric interaction. Scale bar is 50 μm. Shown are exemplary datasets from two technical replicates.

supplemented with 2 M urea, 0.2 M Tris(2-carboxyethyl)phosphine (TCEP), and 1 mM PMSF. Cells were sonicated, and the lysate was centrifuged at 39,000 g to remove further aggregation. The supernatant was incubated with washed Ni beads (1 ml per 2 liters of culture) for 2 h. Proteins were eluted in 2 M urea buffer containing 500 mM imidazole and dialyzed for 24 h to remove the imidazole. Proteins were incubated again with the Ni beads to remove cleaved tag and uncleaved proteins. Final purification was achieved by HPLC. Fractions were analyzed by SDS-PAGE and stained with Coomassie blue. Pure fractions were

pooled and lyophilized overnight. For labeling, samples were exchanged to 4 M GdmHCl and 100 mM NaCl at pH 6.6. Labeling with Alexa Fluor 594 and Alexa Fluor 488 maleimide was done using a twofold molar excess (dye:protein) for 2 h at room temperature. The reaction was quenched with 10 mM DTT, and free unreacted dyes were removed by gel filtration on a Superdex S75 column.

All the small cargoes used in this work were purified from *Escherichia coli* BL21 (DE3) AI cells containing a pBAD-6His and pBAD-12His plasmids for the GFP cargo and the mCherry cargo,

respectively. The cultures were grown overnight with shaking at 37°C and used at a 1:100 dilution to inoculate an expression culture in lysogeny broth medium. Cells were incubated at 37°C with shaking, and protein expression was induced with 0.02% arabinose once the culture reached OD_{600} = 0.6. All the proteins were expressed overnight at 20°C with shaking (180 rpm). Cells were then harvested by centrifugation; pellets were resuspended and lysed with a microfluidizer. The lysate was spun down in a Beckmann centrifuge. The clear lysate was then incubated for 2 h on Ni beads (1 ml for each liter of expression) at 4°C under rotation. Beads were then poured into a polypropylene column and the flow-through was collected. Ni beads were washed with 10 bead volumes of wash buffer (50 mM Tris, pH 7.5, 150 mM NaCl, 0.2% Triton X-100, 10% glycerol, 10 mM imidazole, 0.2 mM TCEP, and 1 mM PMSF) and then with 4 bead volumes of wash buffer (50 mM Tris, pH 7.5, 150 mM NaCl, 0.2% Triton X-100, 10% glycerol, 50 mM imidazole, 0.2 mM TCEP, and 1 mM PMSF). The protein was eluted with 2–3 bead volumes of elution buffer (50 mM Tris, pH 7.5, 150 mM NaCl, 0.2% Triton X-100, 10% glycerol, 500 mM imidazole, 0.2 mM TCEP, and 1 mM PMSF). The elution was concentrated in a centrifugal concentrator filter and, finally, purified via a Superdex S200 column. For long-term storage at −80°C, the protein was flash frozen in liquid nitrogen after adding 25% glycerol.

The mCherry-12His cargo used for the passive exclusion experiment was obtained purifying the flow-through from the first round of Ni beads purification via a Superdex S75 column. The MS2 bacteriophage cargo was purified as previously described (Paci and Lemke, 2019). Briefly, a colony of *E. coli* BL21 (DE3) AI cells containing the pBAD_MS2_Coat_Protein-(1–393) plasmid was inoculated in lysogeny broth medium containing 50 µg/ml ampicillin. Expression was the same as in the small cargoes, but it was performed at 37°C with shaking (180 rpm) for 4 h. Cells were harvested by centrifugation at 4,500 rpm for 20 min at 4°C. For purification, pellets were resuspended in an equal volume of lysis buffer (10 mM Tris, pH 7.5, 100 mM NaCl, 5 mM DTT, 1 mM $MgCl_2$, and 1 mM PMSF) and lysed through three to four rounds in a microfluidizer at 4°C. The lysate was incubated with 0.2% polyethylenimine for 1 h on ice and then clarified by centrifugation at 10,000 rpm with a Beckmann JA 25.50 rotor for 30 min. A saturated solution of $(NH_4)_2SO_4$ was added at 4°C dropwise to the clear lysate under continuous mild stirring, up to a final concentration of 25%. After 1 h, the lysate was pelleted by centrifugation using the same rotor for 30 min. The supernatant was discarded, and the pellets were gently resuspended with 10–20 ml of lysis buffer on a rotator at room temperature. The lysate was then centrifuged again for 30 min, and the clear supernatant was collected. The supernatant was cleared using the KrosFlo system (SpectrumLabs) with a 0.2-µm cutoff membrane to remove large impurities. The sample was then concentrated using the KrosFlo with a 500-kD cutoff membrane. Purified capsids were labeled via maleimide chemistry to couple a fluorescent dye and NLS peptide to the exposed cysteines. The dye (Alexa Fluor 647 maleimide; Invitrogen) and NLS peptide (maleimide-GGGGKTGRLESTPPKKKRKVEDSA; PSL Peptide Specialty Laboratories) were stored at −80°C and freshly resuspended in anhydrous DMSO. The capsids were incubated with different molar excesses of dye and NLS peptide according to the desired degree of labeling for 1–2 h at room temperature. The reaction was then quenched by adding 10 mM DTT, and the protein was pelleted at 10,000 rpm for 10 min to remove any precipitation. The excess dye was removed by loading the sample on a HiPrep Sephacryl S500 16/60 size exclusion column (GE Healthcare). Relevant fractions containing the labeled capsids were then pooled and concentrated using the KrosFlo. For long-term storage at −80°C, the sample was supplemented with 25% glycerol and flash-frozen in liquid nitrogen.

Microfluidic device fabrication and operation

The microfluidic device was made using conventional photolithography techniques. The master mold was fabricated using SU-8-2015 photoresist (Microchem). A 25-µm-thick layer of photoresist was spun on silicon wafer, baked, and exposed to the UV light through a transparency photomask, baked again to cure the UV, and finally developed. The final mold was hard baked and then silanized with chlorotrimethylsilane (Sigma-Aldrich). To obtain the final silicon device, the polydimethylsiloxane (PDMS; Sylgard 184) prepolymer and cross-linking agent (Dow Corning) were mixed at a mass ratio of 10:1 (wt/wt); the mix was poured onto the master and cured at 65°C for ≥2 h. The replica was peeled off the wafer, and inlets and outlets were made by punching the PDMS with a blunt needle. The PDMS was covalently bonded to a standard microscope coverglass by treating both with oxygen plasma.

The microfluidic device presented here was designed to exchange the protein solution to trigger phase separation of Nups ready to be interrogated in the optical region of the device. Buffer exchange occurred at the first mixer (MI) of the device, where the protein solution is squeezed between the two streams of buffer (30% TMAO in PBS) coming from the two side channels (Gambin et al., 2010; Tyagi et al., 2014). The sample channel and the mixing region are 40 and 30 µm wide, respectively, and 20 mm and 50 µm long. The width of the sample solution stream (w_s) was calculated to be 0.5 µm, leading to diffusive exchange between the sample and the buffer solution at a time scale t_{ex} = $(w_f/2)^2/D$, corresponding to the millisecond range for the GdmHCl ($D = 10^{-5}$ cm^2/s). To enable rapid buffer exchange of the FG-Nup49 into PBS, the volumetric flow rate of the buffer was set to be 100-fold of the volumetric flow rate in the FG-Nup channel. Thus, the device can mix the sample and the buffer in a ratio of 1:100. Indeed, numerical simulation indicated that before the sample phase separates into liquid droplets, the concentration of denaturant in the sample is reduced by 90% compared with its original value. That is why the droplets can already form in the first mixer.

The second mixer (MII) was designed to allow the FG-Nup49 droplets to interact with the cargo of interest, while at the same time preventing them from being squeezed by the cargo solution during the assay (which requires a careful adjustment of flow rates to avoid shearing the fragile droplets). To this end, the volumetric flow rate of the cargo solution was designed to be 50-fold lower than the flow in the measurement channel. This design gave us the advantage of interrogating the droplets in the presence of the cargo of interest without squeezing them.

As can be seen in Fig. S1, due to laminar flow and slow mixing by diffusion, large biomolecules from the cargo inlet channel stay largely at the periphery, while diffusion into the central region is small. At the flow rates used, we can detect a concentration of ≈15% in the central region (color coded in blue in Fig. S1). The time it takes to enrich in the droplet is thus a sum of molecules reaching the droplets by diffusion and the time it takes to enter them. Due to the different sizes of the droplets and their different flow speeds in the device, an exact quantitative calculation of both effects separately is not easily achieved. We thus primarily focused on comparing different biological conditions. For example, adding an NLS to a functional import complex adds only <1% in molecular weight, so the diffusional properties are basically unchanged and thus serve as an ideal control.

The formation of the cargo gradient does not lead to droplets fully immersed in a homogeneously concentrated cargo solution. To reach the center of the channel with 50% of the initial cargo concentration flowing in from the cargo inlets, we estimate a channel length of 1 cm would have been required (Fig. S1). However, in such a long channel, traveling FG-Nups will transition to a hydrogel and clog the device during the experiment. Furthermore, our interest was to study the properties of their liquid state. To do so, the observation channel was designed to be 50 μm wide and ≈3 mm long.

Microfluidic device experiments and imaging

To allow visualization of the FG-Nup49 droplets, a small amount (500 nM) of fluorescently labeled FG-Nup49 was premixed with the unlabeled protein before flowing into the device. Depending on the fluorophore present on the cargo, we used FG-Nup49 labeled with either Alexa Fluor 594 or Alexa Fluor 488. For all experiments that included both cargo and NTRs, they were preincubated together for 30 min to allow formation of the import complex.

Facilitated transport experiments (Figs. 2, 4, and S3, A and B) were performed at room temperature on a custom-built epifluorescence microscope equipped with a 10× air objective (NA 0.4) and scientific complementary metal oxide semiconductor cameras (sCMOS ORCA, Hamamatsu) that allowed imaging a large field of view covering of the whole microfluidic chip to monitor the cargo accumulation over time. For experiments investigating the passive exclusion properties of the droplets (Figs. 3 and S3 C), a custom-built confocal microscope was used to obtain better sectioning. The confocal microscope is equipped with a 60× water objective (NA 1.2) and PicoQuant hybrid detectors. The acquisition software employed was custom-written in LabVIEW (National Instruments) for the epifluorescence microscope and SymPhoTime (PicoQuant) for the confocal microscope.

Microfluidic device analysis

To analyze the facilitated transport experiments, a ratiometric analysis of the raw videos was performed with a custom-written Fiji routine, as follows. A mask (Fig. S2 B) was generated by segmenting the FG-Nup49 channel (Fig. S2 A) and applied to the cargo channel (Fig. S2 C) to extrapolate the cargo signal in the region of interest, e.g., in the droplets (Fig. S2 D). Once a clean

cargo signal (I_g) was obtained, this was added to the red signal of the droplets ($I_g + I_r$; Fig. S2 E) and then the ratio between those two ($I_g/(I_g + I_r)$) was calculated for the full video. Fig. S2 F represents a maximum projection of the full ratiometric movie obtained via ImageJ (National Institutes of Health) for representative purposes. The final plots "intensity versus position of droplets" in Fig. 2 were obtained by analyzing in ImageJ 10^5 droplets in the final colorimetric video, with a droplet area of 5–150 μm², traveling along the full device. All final plotting was done using IgorPro (Wavemetrics).

Cell culture

HeLa Kyoto cells were cultured at 37°C in 5% CO_2 atmosphere in DMEM with 1 g/ml glucose (Gibco; 31885023) supplemented with 1% penicillin-streptomycin (Sigma-Aldrich; P0781), 1% L-glutamine (Sigma-Aldrich; G7513), and 10% FBS (Sigma-Aldrich; F7524). The cells were passaged every 2–3 d for a maximum of 15–17 passages. Cells were seeded 1 or 2 d before the experiment at low density (7,000–10,000 cells per well) in a glass-bottom 8-well Lab-Tek II chambered coverglass (Thermo Fisher Scientific, Nunc; 155383).

Permeabilized cell transport assays

Cells for transport assays were rinsed once with 1× PBS and incubated for 10 min at room temperature with 20 nM Hoechst 33342 (Sigma-Aldrich; B2261) to stain the nuclei. Cells were then washed once with transport buffer (1× TB: 20 mM Hepes, 110 mM KOAc, 5 mM NaOAc, 2 mM MgOAc, and 1 mM EGTA, pH 7.3) and permeabilized by incubation for 10 min at room temperature with digitonin (40 μg/ml). Cells were then washed three times with 1× TB supplemented with 5 mg/ml PEG 6000 (Sigma-Aldrich) to avoid osmotic shock. After the final wash, excess buffer was removed, and the transport mix was quickly added to the cells to start the experiment. The transport mix was composed of 1 μM Importin α, 1 μM Importin β, 4 μM RanGDP, 2 μM NTF2, 2 mM GTP, and 0.5 μM cargoes. To allow the import complex to form, the cargo was first preincubated with Importin β and Importin α on ice for at least 10 min, then the rest of the transport mix was added, and the solution was spun down for 10 min at 10,000 rpm to remove any aggregates. For negative controls, some components were left out of the transport mix, as indicated. In passive transport experiments, no transport mix was added but only the cargo of interest in 1× TB + PEG. Each experiment was performed side by side with control cells incubated with fluorescently labeled 70-kD dextran (Sigma-Aldrich; 53471) to confirm nuclear envelope intactness throughout the whole experiment.

Permeabilized cell imaging

All permeabilized cell imaging was performed at room temperature in 1× TB. Confocal imaging of cell experiments was performed either on a Leica SP8 STED 3× microscope using a 63× oil objective (NA 1.40), HyD detectors, and LASX acquisition software or an Olympus FluoView FV3000 with a 40× air objective (NA 0.95), spectral GaAsP detectors, and FV31S-SW acquisition software (for the Traptavidin-GFP-NLS and MS2 cargoes). Illumination and acquisition settings were selected as appropriate for Hoechst/GFP/mCherry imaging.

Online supplemental material

Fig. S1 shows device characterization and phase separation conditions. Fig. S2 shows epifluorescence whole device/chip pipeline analysis. Fig. S3 shows additional cargo controls. Video 1 shows facilitated transport of NLS-MBP-GFP into FG-Nup49 droplets in the presence of Importin β. Video 2 shows negative control of facilitated transport of NLS-MBP-GFP into FG-Nup49 droplets in the absence of Importin β. Video 3 shows negative control of facilitated transport of M9-MBP-GFP into FG-Nup49 droplets in the presence of Importin β. Video 4 shows passive exclusion properties of the liquid state of FG-Nup49 with M9-MBP-GFP cargo. Video 5 shows passive exclusion properties of the liquid state of FG-Nup49 with mCherry-12His cargo. Video 6 shows passive exclusion properties of the liquid state of FG-Nup49 with mCherry cargo.

Acknowledgments

References

Adam, S.A., R.S. Marr, and L. Gerace. 1990. Nuclear protein import in permeabilized mammalian cells requires soluble cytoplasmic factors. *J. Cell Biol.* 111:807–816. https://doi.org/10.1083/jcb.111.3.807

Ader, C., S. Frey, W. Maas, H.B. Schmidt, D. Görlich, and M. Baldus. 2010. Amyloid-like interactions within nucleoporin FG hydrogels. *Proc. Natl. Acad. Sci. USA.* 107:6281–6285. https://doi.org/10.1073/pnas.0910163107

Alberti, S., A. Gladfelter, and T. Mittag. 2019. Considerations and Challenges in Studying Liquid-Liquid Phase Separation and Biomolecular Condensates. *Cell.* 176:419–434. https://doi.org/10.1016/j.cell.2018.12.035

Annunziata, O., N. Asherie, A. Lomakin, J. Pande, O. Ogun, and G.B. Benedek. 2002. Effect of polyethylene glycol on the liquid-liquid phase transition in aqueous protein solutions. *Proc. Natl. Acad. Sci. USA.* 99:14165–14170. https://doi.org/10.1073/pnas.212507199

Au, S., and N. Panté. 2012. Nuclear transport of baculovirus: revealing the nuclear pore complex passage. *J. Struct. Biol.* 177:90–98. https://doi.org/10.1016/j.jsb.2011.11.006

Babcock, H.P., C. Chen, and X. Zhuang. 2004. Using single-particle tracking to study nuclear trafficking of viral genes. *Biophys. J.* 87:2749–2758. https://doi.org/10.1529/biophysj.104.042234

Bachhuber, T., N. Katzmarski, J.F. McCarter, D. Loreth, S. Tahirovic, F. Kamp, C. Abou-Ajram, B. Nuscher, A. Serrano-Pozo, A. Müller, et al. 2015. Inhibition of amyloid-β plaque formation by α-synuclein. *Nat. Med.* 21:802–807. https://doi.org/10.1038/nm.3885

Eibauer, M., M. Pellanda, Y. Turgay, A. Dubrovsky, A. Wild, and O. Medalia. 2015. Structure and gating of the nuclear pore complex. *Nat. Commun.* 6:7532. https://doi.org/10.1038/ncomms8532

Eisele, N.B., A.A. Labokha, S. Frey, D. Görlich, and R.P. Richter. 2013. Cohesiveness tunes assembly and morphology of FG nucleoporin domain meshworks - Implications for nuclear pore permeability. *Biophys. J.* 105:1860–1870. https://doi.org/10.1016/j.bpj.2013.09.006

Elbaum-Garfinkle, S., Y. Kim, K. Szczepaniak, C.C. Chen, C.R. Eckmann, S. Myong, and C.P. Brangwynne. 2015. The disordered P granule protein LAF-1 drives phase separation into droplets with tunable viscosity and dynamics. *Proc. Natl. Acad. Sci. USA.* 112:7189–7194. https://doi.org/10.1073/pnas.1504822112

Ferreon, A.C., M.M. Moosa, Y. Gambin, and A.A. Deniz. 2012. Counteracting chemical chaperone effects on the single-molecule α-synuclein structural landscape. *Proc. Natl. Acad. Sci. USA.* 109:17826–17831. https://doi.org/10.1073/pnas.1201802109

Fisher, P.D.E., Q. Shen, B. Akpinar, L.K. Davis, K.K.H. Chung, D. Baddeley, A. Šarić, T.J. Melia, B.W. Hoogenboom, C. Lin, and C.P. Lusk. 2018. A Programmable DNA Origami Platform for Organizing Intrinsically Disordered Nucleoporins within Nanopore Confinement. *ACS Nano.* 12:1508–1518. https://doi.org/10.1021/acsnano.7b08044

Frey, S., and D. Görlich. 2007. A saturated FG-repeat hydrogel can reproduce the permeability properties of nuclear pore complexes. *Cell.* 130:512–523. https://doi.org/10.1016/j.cell.2007.06.024

Frey, S., R. Rees, J. Schunemann, S.C. Ng, K. Funfgeld, T. Huyton, and D. Gorlich. 2018. Surface Properties Determining Passage Rates of Proteins through Nuclear Pores. *Cell.* 174:202–217.e209.

Fu, G., L.C. Tu, A. Zilman, and S.M. Musser. 2017. Investigating molecular crowding within nuclear pores using polarization-PALM. *eLife.* 6:e28716. https://doi.org/10.7554/eLife.28716

Gambin, Y., C. Simonnet, V. VanDelinder, A. Deniz, and A. Groisman. 2010. Ultrafast microfluidic mixer with three-dimensional flow focusing for studies of biochemical kinetics. *Lab Chip.* 10:598–609. https://doi.org/10.1039/B914174J

Gambin, Y., V. VanDelinder, A.C. Ferreon, E.A. Lemke, A. Groisman, and A.A. Deniz. 2011. Visualizing a one-way protein encounter complex by ultrafast single-molecule mixing. *Nat. Methods.* 8:239–241. https://doi.org/10.1038/nmeth.1568

Grünwald, D., and R.H. Singer. 2010. In vivo imaging of labelled endogenous β-actin mRNA during nucleocytoplasmic transport. *Nature.* 467:604–607. https://doi.org/10.1038/nature09438

Hinz, H.J. 2012. Thermodynamic data for biochemistry and biotechnology. Springer Science & Business Media, Cham, Switzerland.

Hough, L.E., K. Dutta, S. Sparks, D.B. Temel, A. Kamal, J. Tetenbaum-Novatt, M.P. Rout, and D. Cowburn. 2015. The molecular mechanism of nuclear transport revealed by atomic-scale measurements. *eLife.* 4:e10027. https://doi.org/10.7554/eLife.10027

Hülsmann, B.B., A.A. Labokha, and D. Görlich. 2012. The permeability of reconstituted nuclear pores provides direct evidence for the selective phase model. *Cell.* 150:738–751. https://doi.org/10.1016/j.cell.2012.07.019

Jovanovic-Talisman, T., J. Tetenbaum-Novatt, A.S. McKenney, A. Zilman, R. Peters, M.P. Rout, and B.T. Chait. 2009. Artificial nanopores that mimic the transport selectivity of the nuclear pore complex. *Nature.* 457:1023–1027. https://doi.org/10.1038/nature07600

Kapinos, L.E., B. Huang, C. Rencurel, and R.Y.H. Lim. 2017. Karyopherins regulate nuclear pore complex barrier and transport function. *J. Cell Biol.* 216:3609–3624. https://doi.org/10.1083/jcb.201702092

Ketterer, P., A.N. Ananth, D.S. Laman Trip, A. Mishra, E. Bertosin, M. Ganji, J. van der Torre, P. Onck, H. Dietz, and C. Dekker. 2018. DNA origami scaffold for studying intrinsically disordered proteins of the nuclear pore complex. *Nat. Commun.* 9:902. https://doi.org/10.1038/s41467-018-03313-w

Kim, S.J., J. Fernandez-Martinez, I. Nudelman, Y. Shi, W. Zhang, B. Raveh, T. Herricks, B.D. Slaughter, J.A. Hogan, P. Upla, et al. 2018. Integrative structure and functional anatomy of a nuclear pore complex. *Nature.* 555:475–482. https://doi.org/10.1038/nature26003

Konishi, H.A., and S.H. Yoshimura. 2018. Non-FG-Nups, ELYS and Nup35, coordinate an ordered assembly of FG-Nups on the scaffold of the nuclear pore complex. *bioRxiv.* Preprint posted December 26, 2018.

Kosinski, J., S. Mosalaganti, A. von Appen, R. Teimer, A.L. DiGuilio, W. Wan, K.H. Bui, W.J. Hagen, J.A. Briggs, J.S. Glavy, et al. 2016. Molecular architecture of the inner ring scaffold of the human nuclear pore complex. *Science.* 352:363–365. https://doi.org/10.1126/science.aaf0643

Lemke, E.A., Y. Gambin, V. Vandelinder, E.M. Brustad, H.W. Liu, P.G. Schultz, A. Groisman, and A.A. Deniz. 2009. Microfluidic device for single-molecule experiments with enhanced photostability. *J. Am. Chem. Soc.* 131:13610–13612. https://doi.org/10.1021/ja9027023

Levine, Z.A., L. Larini, N.E. LaPointe, S.C. Feinstein, and J.E. Shea. 2015. Regulation and aggregation of intrinsically disordered peptides. *Proc. Natl. Acad. Sci. USA.* 112:2758–2763. https://doi.org/10.1073/pnas.1418155112

Lim, R.Y., B. Fahrenkrog, J. Köser, K. Schwarz-Herion, J. Deng, and U. Aebi. 2007. Nanomechanical basis of selective gating by the nuclear pore complex. *Science.* 318:640–643. https://doi.org/10.1126/science.1145980

Lin, D.H., T. Stuwe, S. Schilbach, E.J. Rundlet, T. Perriches, G. Mobbs, Y. Fan, K. Thierbach, F.M. Huber, L.N. Collins, et al. 2016. Architecture of the symmetric core of the nuclear pore. *Science.* 352:aaf1015. https://doi.org/10.1126/science.aaf1015

Lin, Y., D.S. Protter, M.K. Rosen, and R. Parker. 2015. Formation and Maturation of Phase-Separated Liquid Droplets by RNA-Binding Proteins. *Mol. Cell.* 60:208–219. https://doi.org/10.1016/j.molcel.2015.08.018

Lowe, A.R., J.H. Tang, J. Yassif, M. Graf, W.Y. Huang, J.T. Groves, K. Weis, and J.T. Liphardt. 2015. Importin-β modulates the permeability of the nuclear pore complex in a Ran-dependent manner. *eLife.* 4:e04052. https://doi.org/10.7554/eLife.04052

Marrone, L., H.C.A. Drexler, J. Wang, P. Tripathi, T. Distler, P. Heisterkamp, E.N. Anderson, S. Kour, A. Moraiti, S. Maharana, et al. 2019. FUS pathology in ALS is linked to alterations in multiple ALS-associated proteins and rescued by drugs stimulating autophagy. *Acta Neuropathol.* 138:67–84. https://doi.org/10.1007/s00401-019-01998-x

Milles, S., and E.A. Lemke. 2011. Single molecule study of the intrinsically disordered FG-repeat nucleoporin 153. *Biophys. J.* 101:1710–1719. https://doi.org/10.1016/j.bpj.2011.08.025

Milles, S., K. Huy Bui, C. Köhler, M. Eltsov, M. Beck, and E.A. Lemke. 2013. Facilitated aggregation of FG nucleoporins under molecular crowding conditions. *EMBO Rep.* 14:178–183. https://doi.org/10.1038/embor.2012.204

Milles, S., D. Mercadante, I.V. Aramburu, M.R. Jensen, N. Banterle, C. Köhler, S. Tyagi, J. Clarke, S.L. Shammas, M. Blackledge, et al. 2015. Plasticity of an ultrafast interaction between nucleoporins and nuclear transport receptors. *Cell.* 163:734–745. https://doi.org/10.1016/j.cell.2015.09.047

Mor, A., S. Suliman, R. Ben-Yishay, S. Yunger, Y. Brody, and Y. Shav-Tal. 2010. Dynamics of single mRNP nucleocytoplasmic transport and export through the nuclear pore in living cells. *Nat. Cell Biol.* 12:543–552. https://doi.org/10.1038/ncb2056

Moussavi-Baygi, R., Y. Jamali, R. Karimi, and M.R. Mofrad. 2011. Brownian dynamics simulation of nucleocytoplasmic transport: a coarse-grained model for the functional state of the nuclear pore complex. *PLOS Comput. Biol.* 7:e1002049. https://doi.org/10.1371/journal.pcbi.1002049

Nehrbass, U., H. Kern, A. Mutvei, H. Horstmann, B. Marshallsay, and E.C. Hurt. 1990. NSP1: a yeast nuclear envelope protein localized at the nuclear pores exerts its essential function by its carboxy-terminal domain. *Cell.* 61:979–989. https://doi.org/10.1016/0092-8674(90)90063-K

Ori, A., N. Banterle, M. Iskar, A. Andrés-Pons, C. Escher, H. Khanh Bui, L. Sparks, V. Solis-Mezarino, O. Rinner, P. Bork, et al. 2013. Cell type-specific nuclear pores: a case in point for context-dependent stoichiometry of molecular machines. *Mol. Syst. Biol.* 9:648. https://doi.org/10.1038/msb.2013.4

Paci, G., and E.A. Lemke. 2019. Molecular determinants of large cargo transport into the nucleus. *bioRxiv.* Preprint posted July 6, 2019.

Panté, N., and M. Kann. 2002. Nuclear pore complex is able to transport macromolecules with diameters of about 39 nm. *Mol. Biol. Cell.* 13: 425–434. https://doi.org/10.1091/mbc.01-06-0308

Patel, A., H.O. Lee, L. Jawerth, S. Maharana, M. Jahnel, M.Y. Hein, S. Stoynov, J. Mahamid, S. Saha, T.M. Franzmann, et al. 2015. A Liquid-to-Solid Phase Transition of the ALS Protein FUS Accelerated by Disease Mutation. *Cell.* 162:1066–1077. https://doi.org/10.1016/j.cell.2015.07.047

Ribbeck, K., and D. Görlich. 2002. The permeability barrier of nuclear pore complexes appears to operate via hydrophobic exclusion. *EMBO J.* 21: 2664–2671. https://doi.org/10.1093/emboj/21.11.2664

Schäfer, L. 1999. Excluded volume effects in polymer solutions, as explained by the renormalization group. Springer, Berlin; 554 pp.

Schmidt, H.B., and D. Görlich. 2015. Nup98 FG domains from diverse species spontaneously phase-separate into particles with nuclear pore-like permselectivity. *eLife.* 4:e04251. https://doi.org/10.7554/eLife.04251

Seisenberger, G., M.U. Ried, T. Endress, H. Büning, M. Hallek, and C. Bräuchle. 2001. Real-time single-molecule imaging of the infection pathway of an adeno-associated virus. *Science.* 294:1929–1932. https://doi.org/10.1126/science.1064103

Strawn, L.A., T. Shen, N. Shulga, D.S. Goldfarb, and S.R. Wente. 2004. Minimal nuclear pore complexes define FG repeat domains essential for transport. *Nat. Cell Biol.* 6:197–206. https://doi.org/10.1038/ncb1097

Teimer, R., J. Kosinski, A. von Appen, M. Beck, and E. Hurt. 2017. A short linear motif in scaffold Nup145C connects Y-complex with pre-assembled outer ring Nup82 complex. *Nat. Commun.* 8:1107. https://doi.org/10.1038/s41467-017-01160-9

Timney, B.L., B. Raveh, R. Mironska, J.M. Trivedi, S.J. Kim, D. Russel, S.R. Wente, A. Sali, and M.P. Rout. 2016. Simple rules for passive diffusion through the nuclear pore complex. *J. Cell Biol.* 215:57–76. https://doi.org/10.1083/jcb.201601004

Tu, L.-C., G. Fu, A. Zilman, and S.M. Musser. 2013. Large cargo transport by nuclear pores: implications for the spatial organization of FG-nucleoporins. *EMBO J.* 32:3220–3230. https://doi.org/10.1038/emboj.2013.239

Tyagi, S., V. VanDelinder, N. Banterle, G. Fuertes, S. Milles, M. Agez, and E.A. Lemke. 2014. Continuous throughput and long-term observation of single-molecule FRET without immobilization. *Nat. Methods.* 11: 297–300. https://doi.org/10.1038/nmeth.2809

Wagner, R.S., L.E. Kapinos, N.J. Marshall, M. Stewart, and R.Y.H. Lim. 2015. Promiscuous binding of Karyopherinβ1 modulates FG nucleoporin barrier function and expedites NTF2 transport kinetics. *Biophys. J.* 108: 918–927. https://doi.org/10.1016/j.bpj.2014.12.041

Wei, M.T., S. Elbaum-Garfinkle, A.S. Holehouse, C.C. Chen, M. Feric, C.B. Arnold, R.D. Priestley, R.V. Pappu, and C.P. Brangwynne. 2017. Phase behaviour of disordered proteins underlying low density and high permeability of liquid organelles. *Nat. Chem.* 9:1118–1125. https://doi.org/10.1038/nchem.2803

Yamada, J., J.L. Phillips, S. Patel, G. Goldfien, A. Calestagne-Morelli, H. Huang, R. Reza, J. Acheson, V.V. Krishnan, S. Newsam, et al. 2010. A bimodal distribution of two distinct categories of intrinsically disordered structures with separate functions in FG nucleoporins. *Mol. Cell. Proteomics.* 9:2205–2224. https://doi.org/10.1074/mcp.M000035-MCP201

Zahn, R., D. Osmanović, S. Ehret, C. Araya Callis, S. Frey, M. Stewart, C. You, D. Görlich, B.W. Hoogenboom, and R.P. Richter. 2016. A physical model describing the interaction of nuclear transport receptors with FG nucleoporin domain assemblies. *eLife.* 5:e14119. https://doi.org/10.7554/eLife.14119

Supplemental material

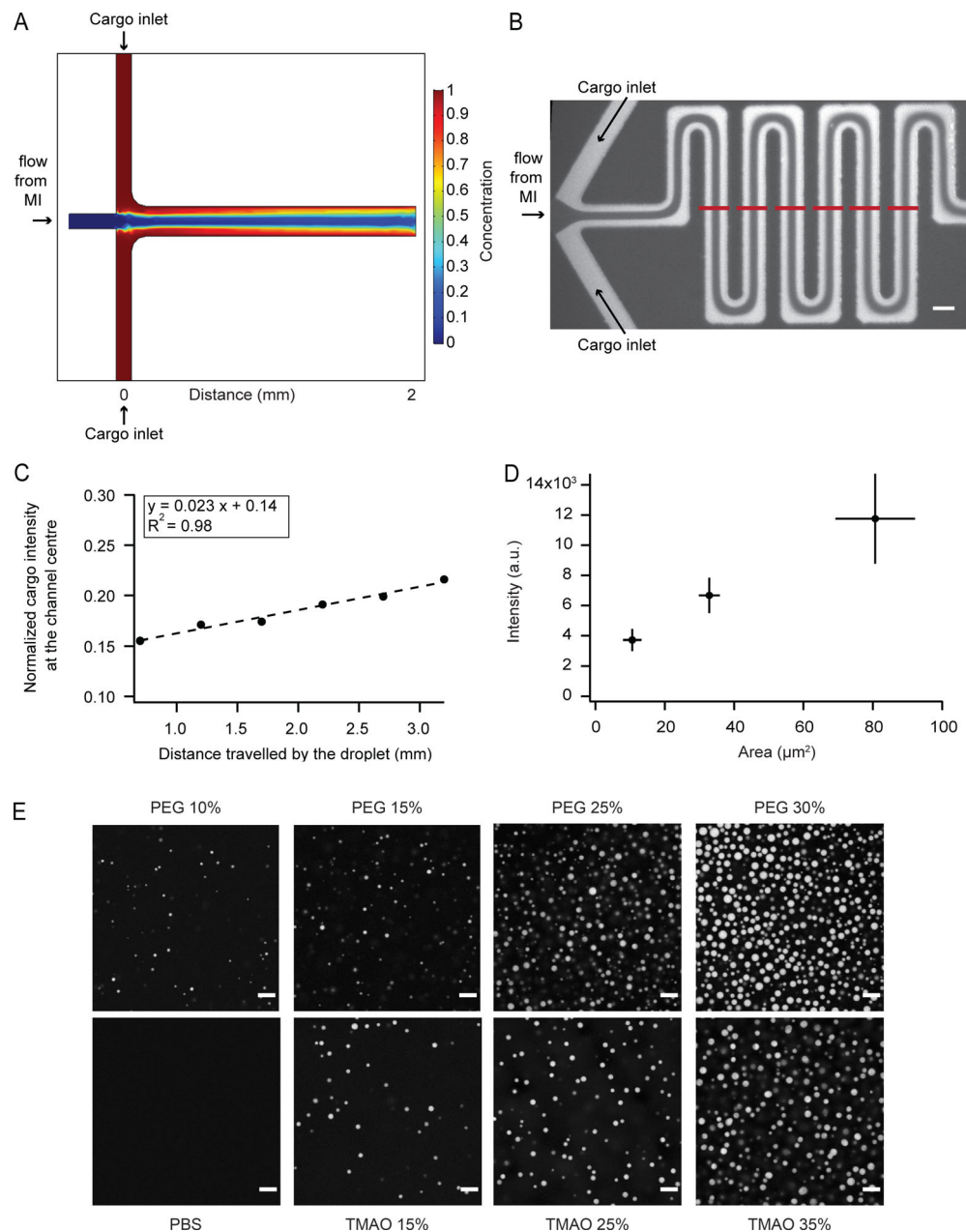**Celetti et al.,** https://doi.org/10.1083/jcb.201907157

Figure S1. **Device characterization and phase separation conditions. (A–C)** Characterization of the diffusion profile inside the microfluidic device. In such laminar flow mixers (MI and MII; Fig. 1), mixing occurs only by diffusion (Gambin et al., 2011; Lemke et al., 2009). To illustrate how such a concentration profile looks, A shows a finite element simulation performed in COMSOL Multiphysics for the second mixer MII. A diffusion coefficient of 10^{-7} cm^2/s ($\approx$ expected diffusion coefficient for molecules of the size of Importin β) was used for the biomolecules perfused in the cargo inlet channels. We also characterized the diffusion profile experimentally: to empirically calculate the concentration of cargo in the center of the main channel, we flowed fluorescently labeled Importin β in the cargo inlet and measured its concentration at different points in the center of the channel. B shows an image of the microfluidic device when only fluorescently labeled Importin β was loaded into the cargo inlet (scale bar is 50 µm), while from mixer MI, only PBS was flowing in the MII region. The red lines indicate positions at which we calculated the ratio of fluorescent Importin β in the center of the channel versus the periphery. The resulting ratio, plotted into C, revealed a slight increase from $\approx$15% to 20% over time/distance traveled. This concentration profile was consistent with the results from the COMSOL simulation. **(D)** Quantification of the FG-Nup49 concentration inside the droplets. Five different dye concentration solutions were first introduced inside the device to obtain an internal calibration curve that was used to estimate the concentration of the droplets based on their fluorescent intensity. For the quantification, 50 individual droplets were analyzed. As the droplets can differ in size, we compared the protein concentration in relation to droplet area (as segmented in ImageJ) and calculated the corresponding percentage polypeptide according to Hinz (2012). **(E)** Experimental phase separation conditions on a coverslip assay. Fluorescence images of phase-separated FG-Nup49 particles formed in presence of different concentration of TMAO or crowder (PEG 8000; scale bar is 10 µm). Lyophilized FG-Nup49 was dissolved in a small volume of stock buffer (4 M GdmHCl and 1× PBS, pH 7.0) and rapidly diluted to a final concentration of 10 µM into 1× PBS containing different concentrations of TMAO or PEG, which yielded similar droplets that were allowed to settle on a coverslip. TMAO was chosen for droplet experiments on the microfluidic device, as it has faster diffusive properties. As in the device experiments, here also FG-Nup49 labeled with Cy5 was added to unlabeled FG-Nup at a very small concentration ($\approx$20 nM) to visualize the self-assembled particles. Images were taken on a confocal microscope, Olympus FV3000, using a 63× oil-immersion objective.
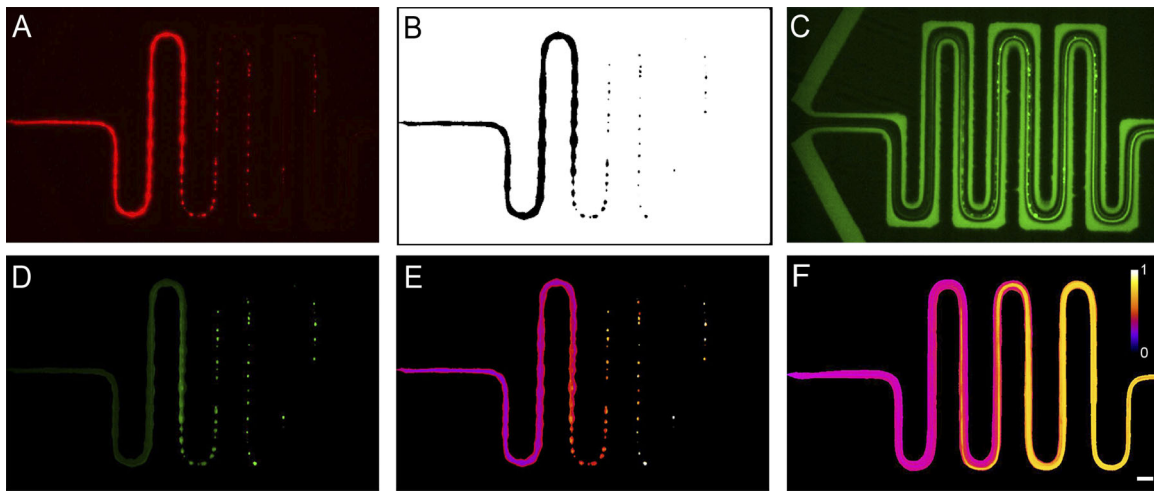
Figure S2. **Epifluorescence whole device/chip pipeline analysis.** This figure summarizes the analysis pipeline to calculate cargo enrichment into the droplets when imaging the whole device using a 10× objective and epifluorescence microscopy. **(A)** Red signal from fluorescence of FG-Nup49 droplets. **(B)** Mask obtained by segmenting the red channel (FG-Nup49). **(C)** Green signal from the cargo fluorescence. **(D)** Signal of the cargo only in the region of interest (droplets region) obtained by applying mask B to image in C. **(E)** Colorimetric image of the ratio between the sum of A and D divided by D. **(F)** Maximum-intensity projection of the full ratio video. Scale bar is 50 μm.
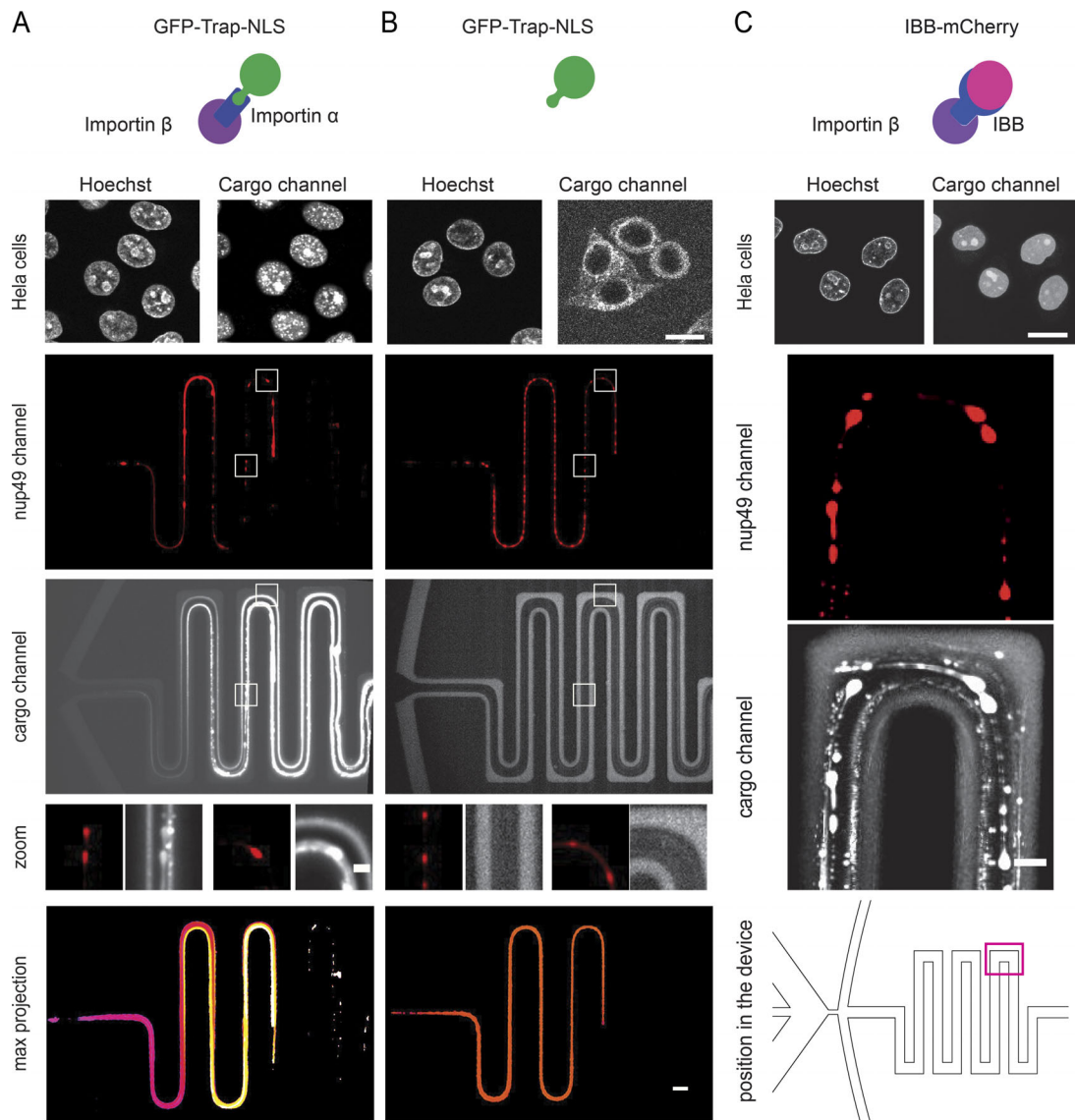
Figure S3. **Additional cargo controls. (A and B)** Facilitated transport of Traptavidin-GFP-NLS in the presence and absence of Importin β/Importin α into the FG-Nup49 droplets studied using a 10× objective and epifluorescence microcopy (whole device). This experiment was particularly challenging because of precipitation of cargo/NTRs complexes inside the device (likely due to the tendency of traptavidin to multimerize). Despite this issue, we could observe a remarkable difference between the experiments in the presence and absence of NTRs (A and B, respectively). The maximum-intensity projection in the figure shows the enrichment of the cargo into the droplets along the device. As for all the facilitated transport experiments shown in this article, the functionality of this cargo was also tested in cells with and without NTRs (top row A and B, respectively). Scale bar is 50 µm. **(C)** Facilitated transport of IBB-mCherry in the presence of Importin β inside the FG-Nup49 droplets studied on a confocal microscope. This is the positive control corresponding to Fig. 3 C. The IBB-mCherry/Importin β mix was preincubated at a 1:1 ratio for 30 min before the start of the microfluidic experiment. The interaction between this cargo and the FG-Nup49 droplets is evident in the cargo channel. The top row shows functionality of the IBB-mCherry cargo in permeabilized cell assays. The last row shows the region of the device in which confocal imaging was performed; all images in Fig. 3 were recorded in this same region. Scale bar is 20 µm, acquired on a custom confocal microscope with a 60× objective (water).
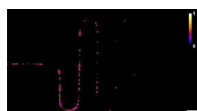
Video 1. **The ratiometric image series of how IBB-MBP-GFP enriches in FG-Nup49 droplets in the presence of Importin β.** Corresponds to Fig. 2 A. Scale bar, 50 µm. Frame rate, 10 frames/s.
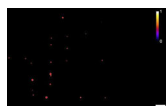
Video 2. **The ratiometric image series of how IBB-MBP-GFP does not enrich in FG-Nup49 droplets in the absence of Importin β.** Corresponds to Fig. 2 B. Scale bar, 50 µm. Frame rate, 10 frames/s.
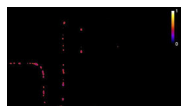
Video 3. **The ratiometric image series of how M9-MBP-GFP does not enrich in FG-Nup49 droplets in the presence of Importin β.** Corresponds to Fig. 2 C. Scale bar, 50 µm. Frame rate, 10 frames/s.

Video 4. **Side-by-side FG-Nup49 channel (left) and M9-MBP-GFP channel (right), revealing a rim stain of the cargo.** Corresponds to Fig. 3 A. Scale bar, 20 µm. Frame rate, 5 frames/s.

Video 5. **Side-by-side FG-Nup49 channel (left) and mCherry-12His channel (right), revealing a rim stain of the cargo.** Corresponds to Fig. 3 B. Scale bar, 20 µm. Frame rate, 5 frames/s.

Video 6. **Side-by-side FG-Nup49 channel (left) and mCherry channel (right), revealing no interaction between the cargo and the FG-Nup droplets.** Corresponds to Fig. 3 C. Scale bar, 20 µm. Frame rate, 5 frames/s.

References

Gambin, Y., V. VanDelinder, A.C. Ferreon, E.A. Lemke, A. Groisman, and A.A. Deniz. 2011. Visualizing a one-way protein encounter complex by ultrafast single-molecule mixing. *Nat. Methods.* 8:239–241. https://doi.org/10.1038/nmeth.1568

Hinz, H.J. 2012. Thermodynamic data for biochemistry and biotechnology. Springer Science & Business Media, Cham, Switzerland.

Lemke, E.A., Y. Gambin, V. Vandelinder, E.M. Brustad, H.W. Liu, P.G. Schultz, A. Groisman, and A.A. Deniz. 2009. Microfluidic device for single-molecule experiments with enhanced photostability. *J. Am. Chem. Soc.* 131:13610–13612. https://doi.org/10.1021/ja9027023